Multi-angular Flame Measurements and Analysis in a Supersonic Wind Tunnel Using Fiber-Based Endoscopes

Lin Ma[1]
Department of Aerospace and Ocean Engineering,
Virginia Tech,
Blacksburg, VA 24061;
Department of Mechanical Engineering,
Virginia Tech,
Blacksburg, VA 24061
e-mail: linma@vt.edu

Andrew J. Wickersham
Department of Mechanical Engineering,
Virginia Tech,
Blacksburg, VA 24061
e-mail: ajwickersham@gmail.com

Wenjiang Xu
Department of Aerospace and Ocean Engineering,
Virginia Tech,
Blacksburg, VA 24061
e-mail: wjxu@vt.edu

Scott J. Peltier
Air Force Research Laboratory,
Dayton, OH 45433
e-mail: scott.peltier.4.ctr@us.af.mil

Timothy M. Ombrello
Air Force Research Laboratory,
Dayton, OH 45433
e-mail: timothy.ombrello.1@us.af.mil

Campbell D. Carter
Air Force Research Laboratory,
Dayton, OH 45433
e-mail: campbell.carter@us.af.mil

This paper reports new measurements and analysis made in the Research Cell 19 supersonic wind-tunnel facility housed at the Air Force Research Laboratory. The measurements include planar chemiluminescence from multiple angular positions obtained using fiber-based endoscopes (FBEs) and the accompanying velocity fields obtained using particle image velocimetry (PIV). The measurements capture the flame dynamics from different angles (e.g., the top and both sides) simultaneously. The analysis of such data by proper orthogonal decomposition (POD) will also be reported. Nonintrusive and full-field imaging measurements provide a wealth of information for model validation and design optimization of propulsion systems. However, it is challenging to obtain such measurements due to various implementation difficulties such as optical access, thermal management, and equipment cost. This work therefore explores the application of the FBEs for nonintrusive imaging measurements in the supersonic propulsion systems. The FBEs used in this work are demonstrated to overcome many of the practical difficulties and significantly facilitate the measurements. The FBEs are bendable and have relatively small footprints (compared to high-speed cameras), which facilitates line-of-sight optical access. Also, the FBEs can tolerate higher temperatures than high-speed cameras, ameliorating the thermal management issues. Finally, the FBEs, after customization, can enable the capture of multiple images (e.g., images of the flow fields at multi-angles) onto the same camera chip, greatly reducing the equipment cost of the measurements. The multi-angle data sets, enabled by the FBEs as discussed above, were analyzed by POD to extract the dominating flame modes when examined from various angular positions. Similar analysis was performed on the accompanying PIV data to examine the corresponding modes of the flow fields. The POD analysis provides a quantitative measure of the dominating spatial modes of the flame and flow structures, and is an effective mathematical tool to extract key physics from large data sets as the high-speed measurements collected in this study. However, the past POD analysis has been limited to data obtained from one orientation only. The availability of data at multiple angles in this study is expected to provide further insights into the flame and flow structures in high-speed propulsion systems. [DOI: 10.1115/1.4031306]

Introduction

Cavity-based flameholders are commonly used for hydrocarbon-fueled, supersonic, ramjet (scramjet) combustors [1]. This is due to the formation of a recirculation zone with a longer fluid mechanical residence time than the core flow of the duct. This enables relatively longer residence time for chemical reactions to occur within the cavity [2]. These types of combustors have previously been demonstrated as a suitable option for dual-mode scramjet flameholding [3,4]. Several variables have been investigated with regard to cavity-based flameholders such as fuel mixing [5] and rich/lean blowoff [5,6], shock propagation [7] and pressure/acoustic oscillations [8,9], qualitative effects of heat release [2,10], fuel injection strategies [2,6,11,12], and velocity field and shear layer interaction [5,13]. There have also been attempts to numerically simulate this combustion geometry to better understand the cavity effect on mixing, total pressure loss, and combustion efficiency [14,15]. Through these works, we can conclude that the geometry containing a downstream ramp with direct cavity fuel injections from the ramp produced the best fuel mixing and most robust combustion at a variety of inlet conditions [2]. A number of experiments have confirmed this finding via planar-laser induced fluorescence of OH, CH_2O, and NO radicals [2,4] and flame chemiluminescence imaging of electromagnetically excited OH (OH*) and CH (CH*) radicals [2]. However, all reports observed large-scale, three-dimensional, or out-of-plane features in the reacting cavity [4,6] or localized emission structures that correlate to flame unsteadiness [2]. These results indicate that the physical mechanism of flameholding and the flame structure not being well-understood [5]. Therefore, it is the effort of this work to expand upon the aforementioned studies and to characterize the dominant flame structure and inherent oscillatory modes with cavity-based combustors at fuel-lean and fuel-rich conditions, by imaging the chemiluminescence from a variety of viewing angles simultaneously.

However, measuring chemiluminescence in practical systems has been a major challenge [16–18]. This challenge is further exacerbated when making multidimensional measurements because they typically require multiple viewing angles and locations in an already space limited system [19–21]. A solution to this issue has been investigated in recent years with the use of FBEs [22–24]. FBEs have a relatively small footprint (~10 mm fiber core) when compared to a standard high-speed camera and they are flexible enough to install in environments with limited optical access. Due to these benefits and the need for multiple perspectives to map the

[1]Corresponding author.

Contributed by the Controls, Diagnostics and Instrumentation Committee of ASME for publication in the JOURNAL OF ENGINEERING FOR GAS TURBINES AND POWER. Manuscript received July 14, 2015; final manuscript received July 30, 2015; published online September 1, 2015. Editor: David Wisler.

flame structure, FBEs were used in this work to record emission from seven different viewing projections.

When using FBEs, there are several critical issues that need to be resolved in order to successfully capture images, including the viewing registration of each FBE, quantification of the degradation of spatial resolution, and signal uniformity and signal linearity of each projection during transmission. Viewing registration is the process of determining the precise position and orientation of each FBE in physical space in order to transform from a three-dimensional world coordinate system to a two-dimensional image system. This work adopted an open source MATLAB tool developed specifically for this purpose, to determine the exact location of each FBE in world coordinates [25]. To account for the spatial resolution or how sharply features in an image can be resolved, a known calibration target was used. Optical fibers have been known to attenuate signals and distort images based on fiber length and position; therefore, care had to be taken to use proper lens systems and precise alignment procedures to minimize these losses. With these practices in place, submillimeter spatial resolution was possible and had also been shown using the same FBE setup as demonstrated in the work by Kang et al. [22]. For more information on the use of FBEs in 3D combustion measurements, see Kang et al. [22].

In the rest of this paper, we first outline the experimental setup, including details of the scramjet facility, testing conditions, as well as the diagnostic hardware used to capture chemiluminescence and PIV images. Second, we outline the numerical methods used to quantify the large coherent intrinsic structures of turbulent combustion. We then discuss the results found from the POD analysis and compare and contrast fuel-lean conditions versus fuel-rich conditions.

Experimental Setup

Flow Facility. The experiments were performed in the supersonic wind tunnel of Research Cell 19 at Wright-Patterson Air Force Base. The facility is capable of operating continuously with peak stagnation conditions of 2860 kPa and 922 K at flow rates up to 15.4 kg/s [2,26]. For the current experiments, a generic cavity configuration was used as shown in Fig. 1. The entire flow path is 15.2 cm wide, and there are two ports in the base of the cavity located 1.9 cm on either side of the symmetry plane to accommodate spark plugs [2]. The two spark plugs were fired simultaneously (approximately 100 mJ/pulse) and served as the sole source to ignite the mixture within the cavity. Fuel (C_2H_4) was injected into the cavity from eleven holes in the cavity closeout ramp. A flow Mach number of 2, corresponding to a flight value of $M_{\text{flight}} \approx 4$, total temperature of approximately 610 K, and total pressure of approximately 483 kPa, was used for all experiments. There was optical access from both the side and top through quartz windows, allowing through multiple views examination of the cavity ignition and burning process. While the entire cavity could be viewed through the side windows, the top window restricted the view to the central 10 cm of the 15.2 cm wide flow path.

Previous supersonic PIV measurements were completed in Research Cell 19's scramjet rig by Tuttle et al. [13] focusing on both reacting and nonreacting conditions. Of the four reacting tests completed, one was for a fuel-lean condition of 56 standard liters per minute (SLPM) of ethylene, whereas another was for a fuel-rich condition of 99 SLPM. It was the intention of this paper to repeat these same conditions with more diagnostics to compare current data with previous data. Various datasets were captured with both PIV and chemiluminescence imaging, and the two sets processed in this work for chemiluminescence are listed in Table 1.

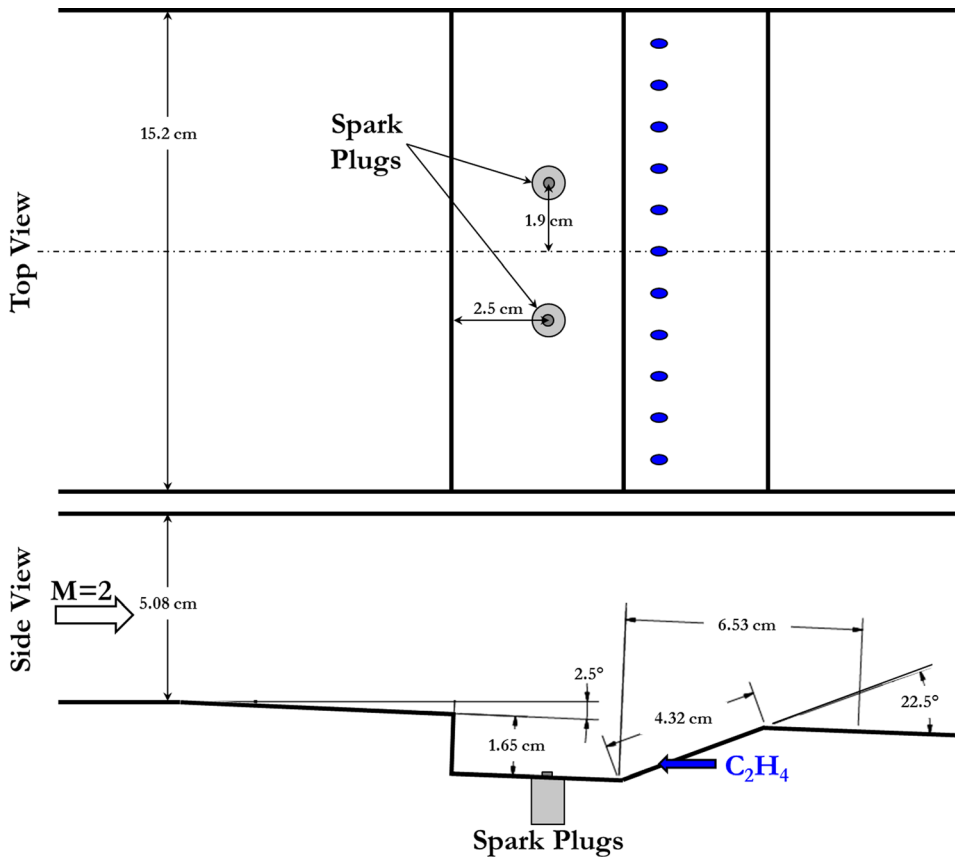

Fig. 1 Schematic of cavity-based flowpath

Table 1 Chemiluminescence testing conditions

Case	1	2
T_0 (F)	636	641
P_0 (psia)	69.9	69.9
Mach	2	2
Fuel flow rate (SLPM[a])	55	95
No. of frames	5000	5000
Frame rate (Hz)	20,000	20,000
Exposure (ms)	0.049	0.049
Total duration (s)	0.245	0.245

[a]SLPM refers to standard liters (referenced to 273 K and 1 standard atm) per minute.

As shown in Table 1, each chemiluminescence case consisted of 5000 total frames; however, this included a portion of the set with no combustion, a small ignition event (83 frames) followed by stable combustion. Only the stable combustion portion was analyzed in this work, which consisted of 4739 frames in total for each case.

Multi-angle Chemiluminescence Sensor. The experimental setup used for measuring combustion chemiluminescence in this scramjet facility is shown in Fig. 2. In this work, a world coordinate system with x along streamwise direction and with y vertical up is employed.

The bottom panel of Fig. 2 shows a photo of one of the FBEs. These FBEs were customized and have been applied in environments with temperature around 60–70 °C. Application under higher temperatures has not been tested yet. Each of the FBE input consisted of an array of 470×470 (220,900) individual single mode fibers, resulting in a total of 883,630 ($4 \times 470 \times 470$) image elements per FBE bundle. Each individual fiber, or image element, has a 17 μm core diameter.

Two high-speed Photron SA-Z cameras were used in combination with two FBE bundles. The customized FBEs as shown in Fig. 2 allow four images be captured by a single camera. Projection image from each FBE inputs is captured by approximately 25% imaging area of the camera (i.e., 512×512 pixels). To clearly show the overall setup position relative to the test section, this figure shows the layout of the chemiluminescence sensor from the cross-sectional view of the tunnel (i.e., the flow is proceeding into the page). Each FBE bundle consisted of one fiber-based output and four fiber-based inputs as shown. Each camera

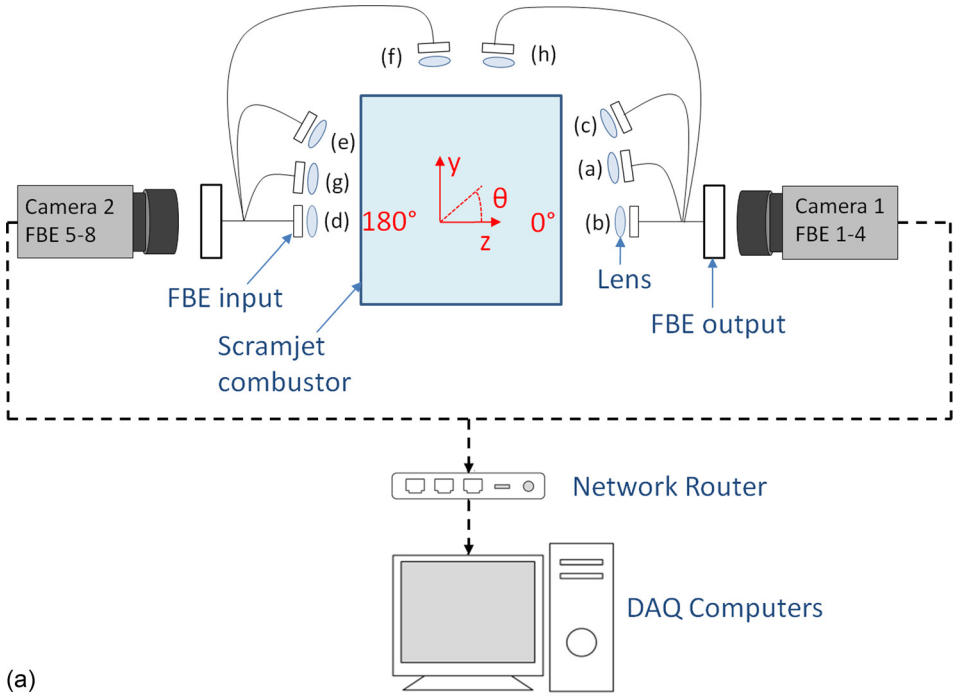

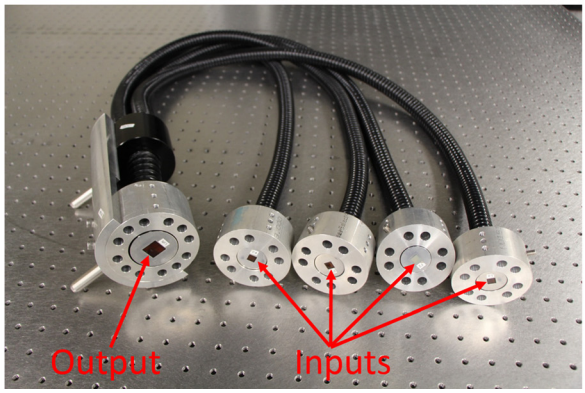

Fig. 2 Top panel: schematic of the experimental setup using eight FBEs to obtain multi-angle chemiluminescence measurements. Bottom panel: a photo of one of the FBEs used.

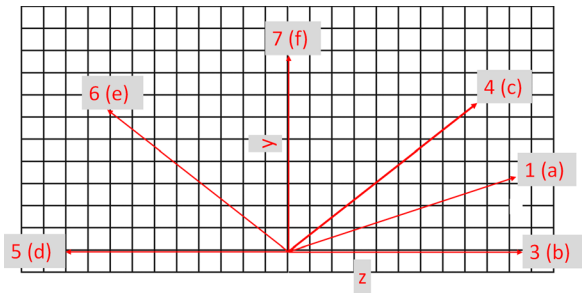

Fig. 3 Orientations of the six FBEs determined from the viewing registration method. The orientations are, respectively: (*a*) FBE1 (17.8 deg), (*b*) FBE3 (0.0 deg), (*c*) FBE4 (38.4 deg), (*d*) FBE5 (180.0 deg), (*e*) FBE6 (144.0 deg), and (*f*) FBE7 (91.9 deg).

was precisely synchronized with the other, and the data were transmitted via a network router and recorded on two data acquisition computers in the adjacent control room.

This work reports the results obtained by six FBEs with orientations as shown in Fig. 3. Note that even though simultaneously chemiluminescence measurements were made from eight orientations as shown in Fig. 2, only six ((*a*)–(*f*)) of the measurements as shown in Fig. 3 were used (and were sufficient) for the POD analysis in this work. Measurements at all the eight orientations are needed for other analysis, such as the 3D reconstruction of the flame structures via tomography (to be reported separately). By using the MATLAB camera calibration toolbox [25] in combination with a calibration target, exact viewing registration angles were calculated. Each FBE was focused onto the same calibration target (from different viewing planes) and from that target, a common focal point was determined. Then each FBE's position and orientation, accounting for spatial degradation, were measured relative to that fixed point in space. The orientations of the FBEs determined using this method are shown in Fig. 3. These orientations are relative to the horizontal direction (z-axis in Fig. 2 and the x-axis is defined to be along the direction of the flow in this work), as calculated using the view registration method originally formulated by Bouguet [25] and demonstrated in Kang et al. [27,28].

An example of the six simultaneous projections, during stable combustion from case 1, is shown in Fig. 4. The chemiluminescence images (as those shown here) were processed with a simple background subtraction (i.e., we read out the signal on each image where no flame was present and subtract it from the image) before used in the POD analysis. The reading of the background signal was on the order of 8, and the peak value of the signal was on the order of 300, resulting in an estimated peak signal to noise ratio of ~37:1. Each image has been oriented such that the flow is proceeding from the left to right. Also, in pictures (*b*), (*d*), and (*f*), lines have been drawn according to the combustor boundaries to help orient the viewer to the precise location of the flame, fuel injection holes, and spark plugs. Each image has been artificially colored based on the same intensity scale (i.e., spatially integrated chemiluminescence signal) of each image, where the color red depicts bright (or most intense) regions and blue indicates areas of no signal. This coloring scheme was adopted for all remaining images in this report.

Both filtered and unfiltered chemiluminescence emissions have been measured in this work, and the results obtained from unfiltered measurements are obtained here. In the filtered measurements, bandpass filters centered at 430 nm (where CH* chemiluminescence peaks) were applied. In the unfiltered measurements, the FBEs themselves only transmit above a wavelength of 400 nm (till about 2 μm) and acted as a wider bandpass filter. The filtered measurements had a significantly lower signal level compared to the unfiltered measurements under the same exposure time, and the results from the POD analysis were similar for both the filtered and unfiltered measurements, as both observed in this work and our previous work [29].

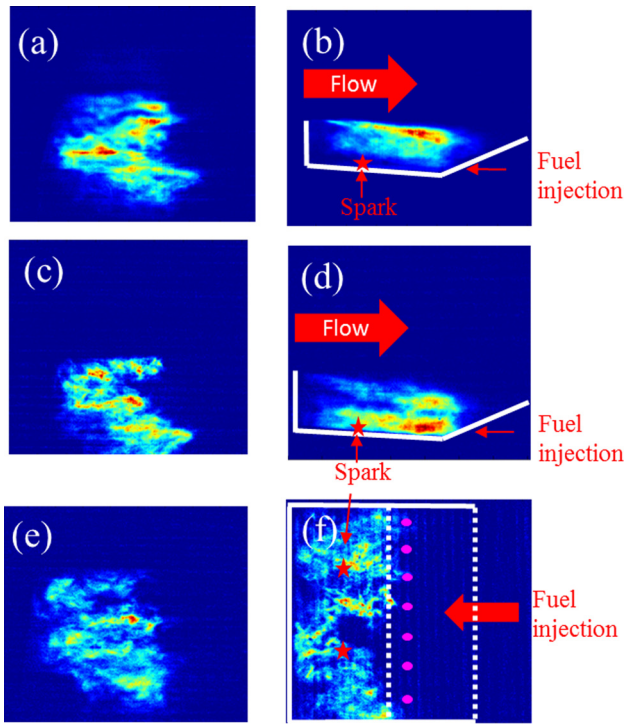

Fig. 4 A set of instantaneous images obtained by the six FBEs simultaneously under the fuel-lean conditions as listed in Table 1

POD. Imaging chemiluminescence with high-speed systems, with or without FBEs, generates large amounts of data, on the order of tens of giga-bytes in fractions of a second. It is important to develop and implement a robust technique capable of reading in every image and quantifying the flame's behavior to allow the objective study of dominant mode shapes and large coherent structures in the flow field. One such technique is the POD, also referred to as principal component analysis or the Karhunen-Loeve expansion. POD can reduce the order of a complex system to a small set of dominant modes that can serve as a lower order representation for the entire data set. This provides data that are more meaningful for increased understanding of turbulent flows in fluid mechanics or heat release distributions when imaging combustion chemiluminescence. POD was first applied to turbulent flows by Lumley and coworkers [30] but to date has been used to understand vorticity in swirl-stabilized combustors [31–34], periodic fluctuations in turbulent shear layers [35,36], vibrational modes in forced resonance systems [37], and fluctuations in V-gutter combustion wakes [38,39]. POD has also recently been used as a means to compare the large outputs from numerical simulations of large eddy simulations to experimental chemiluminescence data for validation purposes [40,41].

There are two common methods of applying POD to numerical or experimental data: classical POD and the method of snapshots. Classical POD is used when the number of variables (or pixels when dealing with images) in the system is less than the number of temporal points or snapshots (number of images in the video set). The method of snapshots, developed by Sirovich [42], is used when there are fewer images in the set than variables. A rigorous mathematical background outlining both methods is available from the von Karman Institute [43]. For our purposes, each FBE is 400×400 pixels (160,000 total pixels/image) and the total number of frames captured in each data set was 5000. Therefore, the method of snapshots is the obvious choice.

By performing the method of snapshots on each set of data, orthogonal modes can be extracted to elucidate the temporal and spatial behavior of the chemically reacting flow. Each mode shape

represents a contribution to the overall flow structure within the combustor volume; therefore, these modes can be used to investigate the key physics underlying the scramjet's operation. POD modes can also be correlated to other synced data, such as pressure transducers to provide insight on specific oscillatory structures that couple with pressure fields that may contribute to Rayleigh gain [44]; however, this was not carried out in the current work. The temporal component of the POD modes can be further analyzed with a fast Fourier transform (FFT) or a continuous wavelet transform to extract more information from the data, such as the dominant frequency each spatial mode oscillates at Ref. [39]. This can be a critical component for understanding the dynamics of turbulent combustion.

This paper focuses on examining the individual POD modes obtained from each FBE, to obtain some form of quantitative measure of flame structure and/or underlying flameholding mechanisms within the supersonic combustor. Moreover, this paper transformed the temporal components of the dominant POD modes to see if there is a characteristic frequency inherent with the combustion and if that frequency is the same or not for each FBE.

Results

Chemiluminescence. POD analysis was completed on both chemiluminescence cases outlined in Table 1 and their results for eigenmodes 1 and 2 are compared in Figs. 5–8, respectively. The first major observation from these results is that the POD analysis yielded different mode shapes depending on the view, which is due to the 3D nature of the flame front in the cavity. The benefit of imaging chemiluminescence from different views enables us to analyze each individual view for conclusions about the global chemical reaction.

One such conclusion is depicted in frame (*b*) of Figs. 5 and 6, which shows the differences in the shear layer flame for the fuel-lean versus the fuel-rich condition. In the fuel-lean condition there is a singular dominant structure centered in the shear layer, whereas for the fuel-rich case, there are two coherent structures dominating the shear layer and impingement region, respectively.

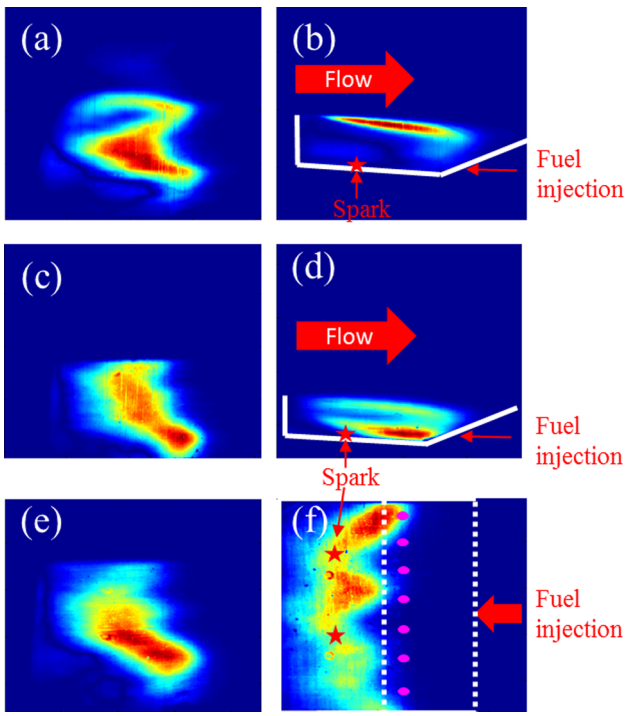

Fig. 5 First eigenmode of fuel-lean flame

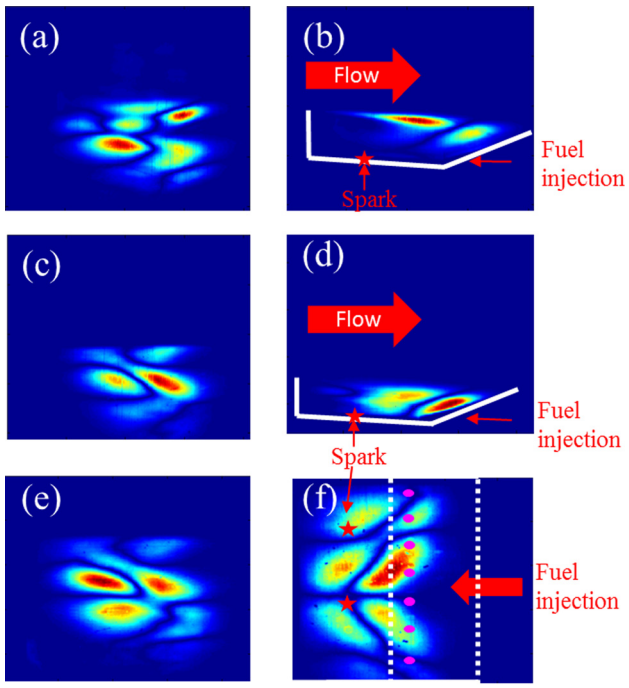

Fig. 6 First eigenmode of fuel-rich flame

This duality of structures is indicative of nonuniform combustion occurring within the cavity.

Other studies, performed with similar conditions and geometry, theorized that a fuel-rich lobe forms on either side of the spanwise centerline, leading to very poor combustion in the upstream end of the cavity coupled with nonuniform burning in the downstream portion of the cavity [2]. This low-temperature fuel-rich region in the upstream cavity section thus inhibits the shear layer from being ignited [2]. The later point is visualized in Figs. 5 and 6

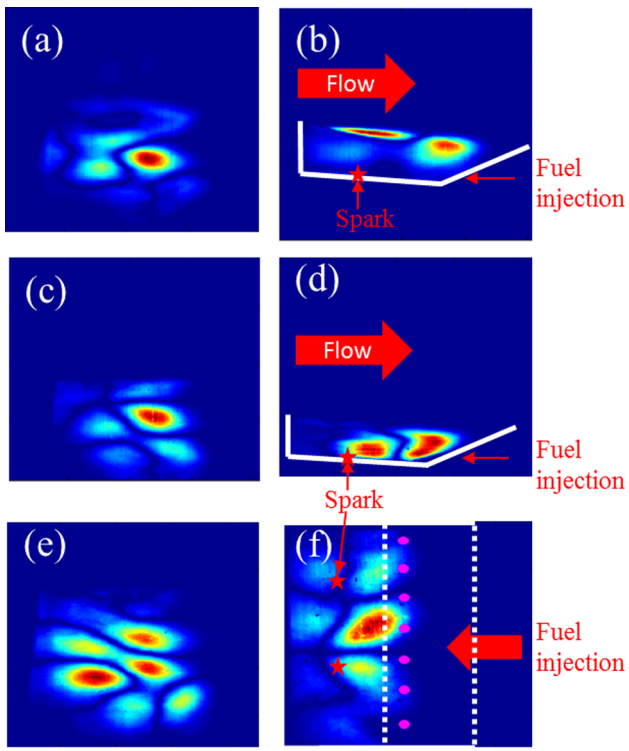

Fig. 7 Second eigenmode of fuel-lean flame

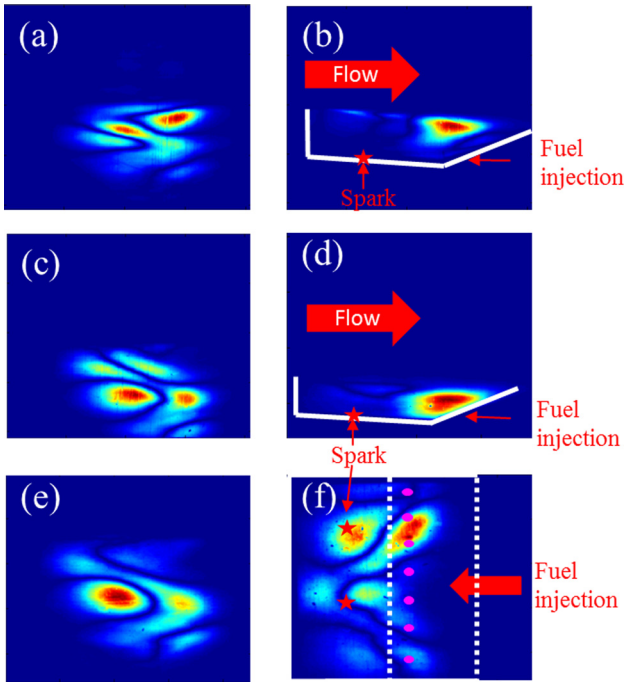

Fig. 8 Second eigenmode of fuel-rich flame

when comparing the size and shape of the flame structure (red colored region) as well as the relative energy content contained within each eigenmode. The relative energy percentage of each eigenmode is determined by the dividing each corresponding eigenvalue by the sum of all of the eigenvalues in the problem.

In physical terms, this is a measure of the variance weight of a structure relative to other structures found by the POD analysis. The relative energy of the first mode of the fuel-lean case is 44.3%, whereas the fuel-rich case was 16.0%, indicating a more stable variant structure in the fuel-lean condition. Coupled with the low relative energy content was the shorter and wider flame structure in the fuel-rich case. Upon closer examination of the instantaneous images in fuel-rich set, the shear layer flame was observed to stabilize prominently in the shear layer, similar to the fuel-lean case, but then periodically blow out and relight from the impingement section.

Another conclusion is the verification that as fuel flow rates increase from low to high fuel loading, the stable combustion region shifts farther downstream in the cavity [5,13,45]. This is indicative in every image of Figs. 7 and 8, but most clearly in panel (*b*) (side view) and (*f*) (top view). From panel (*b*), it can be seen that the region with strong CH* emissions was pushed and further downstream and shrank under fuel-rich condition compared to fuel-lean condition, indicating the requirement for more time to properly mix and, ignite, and burn the mixture. This is also easily observed in a side-by-side comparison between instantaneous images of the top view FBE as well. From panel (*f*), it can be seen that the center portion of the reaction zone has shifted slightly aft, whereas the wings (or flame structures closest to the combustor walls) drastically moved downstream.

The last conclusion drawn from the spatial eigenmodes was the change in flame shape as the fuel loading was increased. Directly comparing images (*c*) and (*e*) in Fig. 5 for fuel-lean conditions to Fig. 6 for fuel-rich conditions, a clear change in structure is evident. The flame structure appears more uniform and linear in the fuel-lean condition, but in the fuel-rich condition changes into a nonlinear structure resembling an "S" or an "M" depending on the viewing angle. This nonlinear structure was observed to persist for periods of time during stable combustion and then dissipate, oscillating between the two modes. This could be indicative of a closed-loop thermoacoustic disturbance, where the heat release

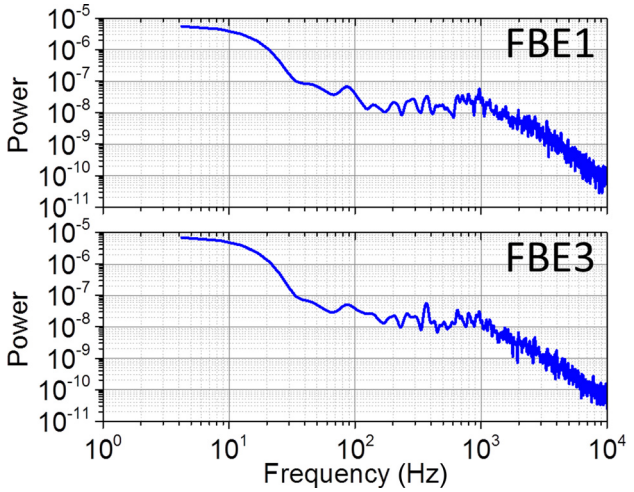

Fig. 9 Power spectrum of fuel-lean conditions from FBE1 (top panel) and FBE3 (bottom panel)

couples with the acoustical field fluctuations, but more information is needed via synchronized pressure measurements to validate this claim.

Analyzing the power spectrum of the dominant temporal coefficients in the POD analysis also yielded some insight into the behavior of cavity-based flame. First, it was observed that the power spectrum obtained was less sensitive to the particular viewing angle as compared to the spatial eigenmodes themselves. For example, when the temporal coefficients (a_1) associated with the first eigenmode were processed with an FFT, the resulting power spectral densities from differing FBEs were quantitatively similar. Figure 9 shows the power spectral densities of FBE1 and FBE3, corresponding to angles 17.8 deg and 0.0 deg, respectively, for the fuel-lean case. The images were taken at a frame rate of 20 kHz; therefore, the single-sided amplitude spectrum could resolve frequencies up to 10 kHz. There appears to be no clear indication of a characteristic frequency, and the spectra appear quantitatively similar, confirming that the frequency content of line-of-sight-averaged chemiluminescence is independent of the orientation as intuitively expected.

Second, it was observed that the power spectral densities differed as the fuel-loading changed. The a_1 temporal coefficients were again processed with an FFT, but for differing fuel cases and identical FBEs. Figure 10 shows the power spectrum of FBE 8 for

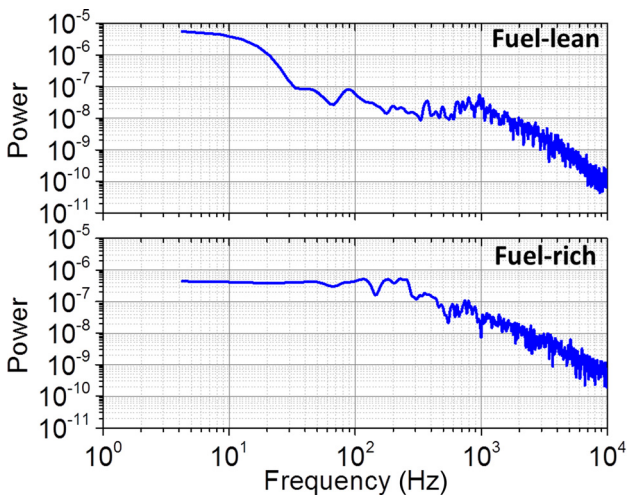

Fig. 10 Power spectrum of FBE 8 for fuel-lean (upper) and fuel-rich (lower) conditions

the fuel-lean case compared to the fuel-rich case. The spectra are qualitatively and quantitatively different. This relationship has been previously observed in subsonic and supersonic combustion with V-gutter, blunt-body combustion, and the similar geometry combustor as shown in this work, respectively, [8,9,29].

PIV Results. In the previous section of Chemiluminescence Results, the POD analysis was used to describe the underlying spatial structure of the reacting cavity flowfield. In order to provide a conceptual link between this behavior and the kinematic state of the fluid, the chemiluminescence eigenmodes were compared with the corresponding basis functions extracted from planar velocimetry. The fuel-lean and fuel-rich velocity fields are taken from the experimental study by Tuttle et al. [13]. While the velocimetry and chemiluminescence were not collected simultaneously, the measurements were performed under nearly identical conditions, and thus provide complementary descriptions of the flow structure.

The velocity data was collected by PIV, yielding instantaneous velocity fields in the x–y plane along the cavity centerline. Titanium oxide (TiO_2) tracer particles were introduced into the incoming boundary layer approximately 17 cm upstream of the cavity through a low-angled injector port. The particles were illuminated by a dual-head NewWave Solo pulsed Nd:YAG laser operating at 15 Hz. A combination of spherical and cylindrical lenses elongated the 532 nm beam into a quasi-two-dimensional sheet approximately 0.5 mm thick. The laser sheet was then passed vertically into the test cell at the tunnel centerline ($z = 0$). The time separation Δt between the laser pulses was 2.2 μs, and the resultant Mie scattering from the particles was collected by a Cooke PCO 1600 interline-transfer CCD camera. Flame emission was blocked by a bandpass filter (Semrock) with a 532 nm center wavelength and 3 nm spectral width. Due to limitations in the onboard camera memory and tunnel running time, 425 image pairs were collected for each condition. Uncertainty levels remained below 3 m/s for a majority of the flowfield, though higher values near 7 m/s were observed where the shear layer impinges onto the closeout ramp. For a more detailed description of the PIV experimental arrangement, see Ref. [13].

The particle images were processed into velocity fields by LaVision DaVis Flowmaster v7.2, using multipass cross-correlations on interrogation windows of size 128, 64, and 32 pixels. For each window size, the cross-correlations were repeated twenty times to improve convergence, and the interrogation windows were overlapped by 50% to improve the final vector spacing. The dimensional size of the final interrogation window is 1.81 mm, yielding a vector spacing of 0.906 mm (including the 50% overlap).

The ensemble-averaged velocity fields of the fuel-lean and fuel-rich cases are shown in Fig. 11. Contours of the streamwise velocity U are plotted, and estimated pathlines are overlaid to indicate the local flow direction. Both cases indicate a clearly visible recirculation region near the closeout ramp, which acts as the primary large-scale mixing mechanism for distributing unburnt reactants within the cavity. The pathlines were computed by integrating the ensemble-averaged velocity. The centroid of the recirculation zone is centered at $x = 58$ mm for the fuel-lean case, but is shifted upstream to $x = 52$ mm under fuel-rich conditions. Despite this change in the recirculation centroid, the remainder of the cavity is remarkably similar between the two fueling cases for the streamwise as well as (not shown) wall-normal velocity components.

Prior to making any comparisons between the PIV and chemiluminescence eigenmodes, it is important to recall several key features of the POD method. As stated above, the eigenmodes are optimal in the sense that they capture more energy than any other set of basis functions, where the energy is based upon the mean-subtracted data. The energy is defined as the sum of the squares of the fluctuating value. For example, a two-dimensional velocity field would yield modes that are optimized for the two-dimensional, incompressible, turbulent kinetic energy. The instantaneous fluctuating field I' can then be computed as a sum of the

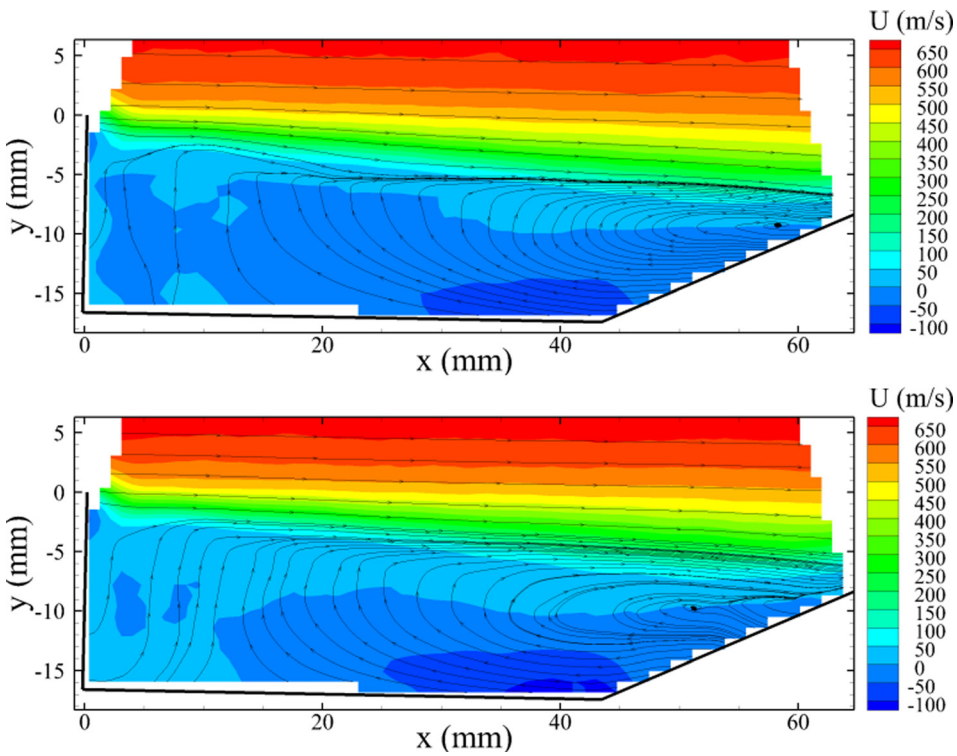

Fig. 11 Ensemble-averaged velocity fields for fuel-lean (upper) and fuel-rich (lower) conditions with overlaid estimated pathlines

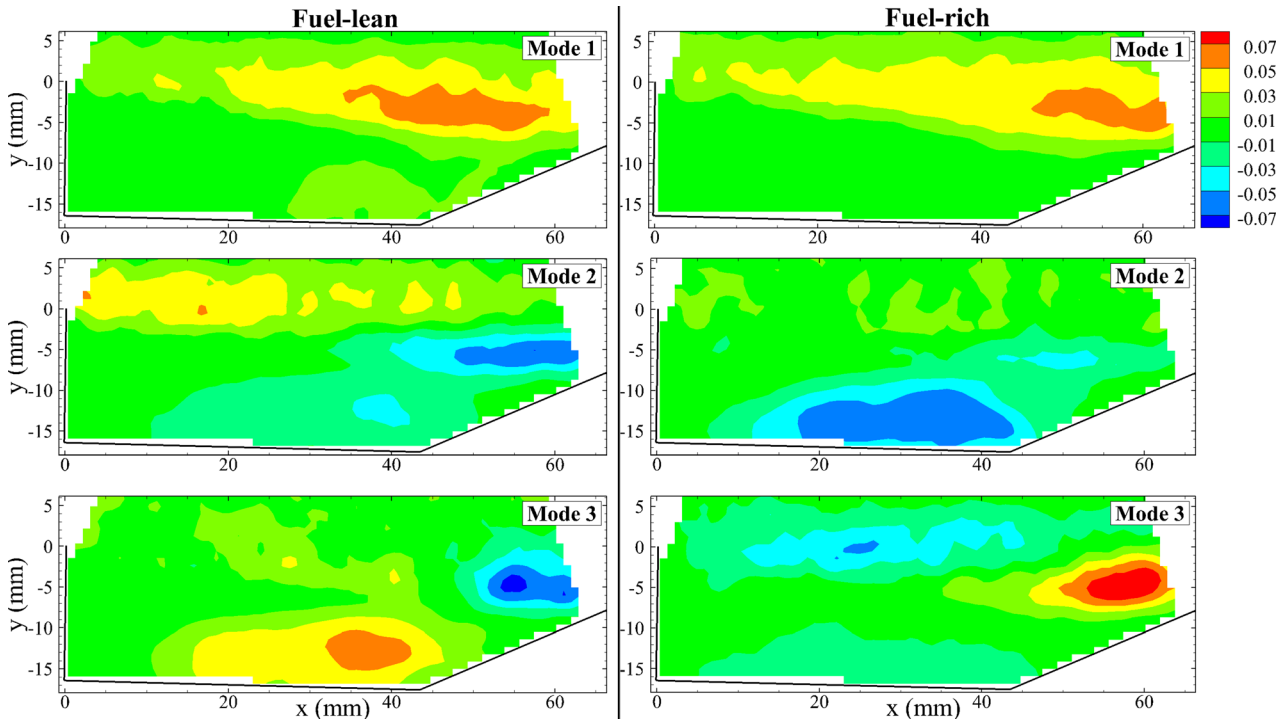

Fig. 12 First four PIV eigenmodes for fuel-lean (left) and fuel-rich (right) conditions

eigenmodes, $\Phi_i(x,y)$, weighted by the temporal coefficients, $a_i(t)$. Using Reynolds decomposition, the instantaneous field I can be represented as

$$I(t) = I_0 + \sum_{i=1}^{\#\text{modes}} \Phi_i(x,y)a_i(t)$$

Therefore, an individual eigenmode does not describe the components of the mean flow, but instead shows the contributions to the deviations from the mean for each frame, $I(t)$. This distinction is important as we discuss the basis functions computed from the velocity fields.

The first three eigenmodes of the velocity fields are shown in Fig. 12 for the fuel-lean and fuel-rich cases. Poorly seeded regions have been masked, so as not to contaminate the calculation of the eigenmodes. The POD analysis was performed simultaneously for both the streamwise and wall-normal velocity.

A comparison of both velocity components (not shown) has shown that the basis functions describe similar structures, and hence only the U eigenmodes are plotted here. In all cases, the modulus of each eigenmode has been normalized to unity, such that $\|\Phi_u(x,y)\| = 1$. The resultant modes are plotted on an arbitrary scale in Fig. 12. The weighting coefficients, $a_i(t)$, may assume both positive and negative values, resulting in a positive or negative contribution of each basis function to the instantaneous fluctuating field. Similarly, the values within the modes also span both positive and negative values. The limited sample size and low-repetition rate of the velocimetry data do not allow a quantitative description of the basis functions or their respective temporal coefficients. However, an inspection of each mode can indicate the relative contributions of the underlying structure.

The convergence of the PIV eigenmodes was examined by repeating the POD computation for successively smaller subsets of the sample size N. The energy content of each mode varied by less than 1% for data sets in the range $N = 275$–425. Additionally, the mode shapes of the smaller subsets (not shown) were constant for $N > 300$. Based upon these observations, the sample size $N = 425$ is considered to be sufficient for convergence.

The purpose of decomposing the PIV velocity fields into eigenmodes is to identify the effects of combustion and heat release upon the velocity fluctuations (only the axial fluctuations are considered in this discussion). While the streamwise velocity fluctuations may be described by the axial stress $\overline{u'u'}$, it is difficult to parse the contributions of the salient flow structures (e.g., shear layer, shear layer impingement, recirculation zone) due to the proximity of these features. The POD technique provides an objective method for distinguishing the contributions of these flow structures to the ensemble-averaged stress. In the current analysis, only the spatial structure of the axial stress is discussed, corresponding to the shapes of the eigenmodes. The quantitative contributions of each mode to the axial stress may be determined by inspecting the temporal coefficients, though this analysis is not included in the current discussion.

Prior to analyzing the sensitivity of the eigenmodes to fueling rate, it is necessary to establish a connection between the mode-shapes and the cavity flow structures using the first three modes of the fuel-lean case in Fig. 12. Mode 1 exhibits a broad active region over the closeout ramp, corresponding to the position of the cavity shear layer. Recall from previous discussions that POD is performed on the fluctuating field (u', v'), and therefore the first axial eigenmode Φ_u describes the distribution of the streamwise fluctuations within the shear layer. The second fuel-lean mode shows a weakly active region near the cavity step, coincident with the upstream shear layer. However, the majority of the motion is concentrated along the closeout ramp. A comparison with the ensemble-averaged velocity in Fig. 11 suggests that this region is due to the shear layer impingement onto the cavity ramp. The third eigenmode exhibits a small active region near the cavity ramp (similar to the shear layer impingement in mode 2), though the largest region occurs along the cavity floor. This area corresponds to the upstream-induced ($U < 0$) flow beneath the recirculation region, as fluid is transported away from the ramp toward the upstream step. Therefore, the third eigenmode describes the fluctuations in this fluid transport. While some of the cavity flow features are described by multiple mode-shapes (e.g., shear layer impingement is visible in both modes 2 and 3 of the fuel-lean case), it is still possible to

describe these motions through the behavior of their respective modes. For the sake of clarity, the first three eigenmodes will be hereafter referred to as the *shear layer mode*, *impingement mode*, and *recirculation mode*. Note that the eigenmodes of the fuel-rich case also contain these same features, though the order of the *impingement* and *recirculation* modes has been reversed. An inspection of the energy content (computed as the respective eigenvalue divided by the sum of all eigenvalues) shows only a 1% difference between modes 2 and 3, and therefore this reversal in order is considered inconsequential for the current discussion.

The first eigenmode in Fig. 12, corresponding to the most dominant (energywise) structure, is remarkably similar for both fueling cases. Both modes suggest that the most active region of the shear layer occurs in the downstream half of the cavity. Closer inspection reveals that the energy content within the shear layer (described by the distribution of the *shear layer mode*) has shifted downstream with the higher fueling rate. This trend is consistent with the chemiluminescence results, which have shown that the combustion zone stabilizes further downstream in the cavity with increased fueling. A similar downstream shift is observed for the upstream portion of the shear layer in the *impingement mode*. However, the most notable feature of the *impingement mode* is the broadened impingement region for the fuel-rich case, as described by the active area along the closeout ramp. This suggests that the heat release near the ramp has increased the shear layer thickness at higher fuel loading, consistent with the findings of Ref. [13]. The *recirculation mode* appears to demonstrate none of the above-mentioned sensitivities to fueling rate within the region of upstream-induced ($U < 0$) flow along the cavity floor. Indeed, the distribution of the active region along the cavity floor is nearly identical for both fueling rates. This motion is strongly linked to the primary recirculation zone beneath the shear layer, as evidenced by the spiraling pathlines around the recirculation centroid in Fig. 11. Therefore, the eigenmodes suggest that the fluctuations of the cavity recirculation (and hence the transport of fluid away from the cavity ramp) do not change appreciably with fueling rate.

The above discussion has demonstrated the utility of POD in distinguishing the behaviors of the cavity flow structures based upon the shapes of the eigenmodes. This method provides an effective approach to analyze the response of the cavity flowfield, and complements an inspection of the ensemble-averaged stresses.

Conclusion

A cavity-based flameholder fueled from the closeout ramp was characterized using multiple perspective chemiluminescence at Mach 2 inlet conditions. These data were combined with the previously obtained PIV to understand the interplay between combustion and the flow field. The multiple perspective chemiluminescence was possible using two 4×1 optical fiber bundles coupled with high-speed cameras, which yielded seven total perspectives in this experiment due to one fiber not being used.

Analysis of the data measured at 20 kHz for a duration of 0.25 s per condition using POD in combination with a FFT yield the following major observations.

(1) The dominant eigenmode structures differed depending on the FBE perspective, which is indicative of the 3D composition of the flame front.
(2) These dominant structures were confirmed from various perspectives to embody nonuniform features that would shift farther downstream with increasing fuel rates as indicated by previous studies.
(3) The power spectra obtained from the same temporal coefficients differed as a function of fuel flow rate, as observed from previous studies.

Acknowledgment

This work was supported by the U.S. Air Force Office of Scientific Research with Dr. Chiping Li as technical monitor. This research was performed while Scott Peltier held a National Research Council Research Associateship Award at the U.S. Air Force Research Laboratory. The authors would like to thank Dr. Steven G. Tuttle (U.S. Naval Research Laboratory) for providing the PIV data. Andrew Wickersham and Lin Ma are also grateful, respectively, for a Rolls-Royce Fellowship and a U.S. Air Force Summer Faculty Fellowship.

Nomenclature

$a_i(t)$ = ith temporal coefficient
$I(t)$ = instantaneous field variable
I_0 = mean field variable
M_{flight} = flight Mach number
P_0 = stagnation pressure
T_0 = stagnation temperature
U = mean streamwise velocity
u' = streamwise velocity fluctuation
$\Phi_i(x,y)$ = ith eigenmode

Abbreviations

FBE = fiber-based endoscope
POD = proper orthogonal decomposition
SLPM = standard liters per minute

References

[1] Ben-Yakar, A., and Hanson, R. K., 2001, "Cavity Flame-Holders for Ignition and Flame Stabilization in Scramjets: An Overview," J. Propul. Power, **17**(4), pp. 869–877.
[2] Gruber, M. R., Donbar, J. M., Carter, C. D., and Hsu, K.-Y., 2004, "Mixing and Combustion Studies Using Cavity-Based Flameholders in a Supersonic Flow," J. Propul. Power, **20**(5), pp. 769–778.
[3] Gruber, M. R., Baurle, R. A., Mathur, T., and Hsu, K. Y., 2001, "Fundamental Studies of Cavity-Based Flameholder Concepts for Supersonic Combustors," J. Propul. Power, **17**(1), pp. 146–153.
[4] Hammack, S. D., Lee, T., Hsu, K.-Y., and Carter, C. D., 2013, "High-Repetition-Rate OH Planar Laser-Induced Fluorescence of a Cavity Flameholder," J. Propul. Power, **29**(5), pp. 1248–1251.
[5] Rasmussen, C. C., Dhanuka, S. K., and Driscoll, J. F., 2007, "Visualization of Flameholding Mechanisms in a Supersonic Combustor Using PLIF," Proc. Combust. Inst., **31**(2), pp. 2505–2512.
[6] Rasmussen, C. C., Driscoll, J. F., Hsu, K. Y., Donbar, J. M., Gruber, M. R., and Carter, C. D., 2005, "Stability Limits of Cavity-Stabilized Flames in Supersonic Flow," Proc. Combust. Inst., **30**(2), pp. 2825–2833.
[7] Choi, J.-Y., Ma, F., and Yang, V., 2005, "Combustion Oscillations in a Scramjet Engine Combustor With Transverse Fuel Injection," Proc. Combust. Inst., **30**(2), pp. 2851–2858.
[8] Ma, F., Li, J., Yang, V., Lin, K.-C., and Jackson, T. A., 2005, "Thermoacoustic Flow Instability in a Scramjet Combustor," AIAA Paper No. 2005-3824.
[9] Lin, K.-C., Jackson, K., Behdadnia, R., Jackson, T. A., Ma, F., and Yang, V., 2010, "Acoustic Characterization of an Ethylene-Fueled Scramjet Combustor With a Cavity Flameholder," J. Propul. Power, **26**(6), pp. 1161–1169.
[10] Rasmussen, C. C., Driscoll, J. F., Carter, C. D., and Hsu, K. Y., 2005, "Characteristics of Cavity-Stabilized Flames in a Supersonic Flow," J. Propul. Power, **21**(4), pp. 765–768.
[11] Allen, W. H., Jr., 2005, "Fuel-Air Injection Effects on Combustion in Cavity-Based Flameholders in a Supersonic Flow," M.S. thesis, Air Force Institute of Technology, Wright-Patterson AFB, OH, p. 104.
[12] Hsu, K.-Y., Carter, C., Gruber, M., Barhorst, T., and Smith, S., 2010, "Experimental Study of Cavity-Strut Combustion in Supersonic Flow," J. Propul. Power, **26**(6), pp. 1237–1246.
[13] Tuttle, S. G., Carter, C. D., and Hsu, K.-Y., 2014, "Particle Image Velocimetry in a Nonreacting and Reacting High-Speed Cavity," J. Propul. Power, **30**(3), pp. 576–591.
[14] Kim, K. M., Baek, S. W., and Han, C. Y., 2004, "Numerical Study on Supersonic Combustion With Cavity-Based Fuel Injection," Int. J. Heat Mass Transfer, **47**(2), pp. 271–286.
[15] Peterson, D. M., Hagenmaier, M., Carter, C. D., and Tuttle, S. G., 2013, "Hybrid Reynolds-Averaged and Large-Eddy Simulations of a Supersonic Cavity Flameholder," AIAA Paper No. 2013-2483.
[16] Ballester, J., and García-Armingol, T., 2010, "Diagnostic Techniques for the Monitoring and Control of Practical Flames," Prog. Energy Combust. Sci., **36**(4), pp. 375–411.

[17] Bheemul, H., Lu, G., and Yan, Y., 2002, "Three-Dimensional Visualization and Quantitative Characterization of Gaseous Flames," Meas. Sci. Technol., **13**(10), p. 1643.
[18] Ma, L., Sanders, S., Jeffries, J., and Hanson, R., 2002, "Monitoring and Control of a Pulse Detonation Engine Using a Diode-Laser Fuel Concentration and Temperature Sensor," Proc. Combust. Inst., **29**(1), pp. 161–166.
[19] Ma, L., Cai, W. W., Li, X., Sanders, S. T., Caswell, A. W., Sukesh, R., Plemmons, D. H., and Gord, J. R., 2012, "50 KHz Rate 2D Imaging of Temperature and H_2O Concentration at Exhaust Plane of J85 Engine by Hyperspectral Tomography," Opt. Express, **21**(1), pp. 1152–1162.
[20] Li, X., and Ma, L., 2014, "Volumetric Imaging of Turbulent Reactive Flows at KHz Based on Computed Tomography," Opt. Express, **22**(4), pp. 4768–4778.
[21] Cai, W., Li, X., Li, F., and Ma, L., 2013, "Numerical and Experimental Validation of a Three-Dimensional Combustion Diagnostic Based on Tomographic Chemiluminescence," Opt. Express, **21**(6), pp. 7050–7064.
[22] Kang, M., Wu, Y., and Ma, L., 2014, "Fiber-Based Endoscopes for 3D Combustion Measurements: View Registration and Spatial Resolution," Combust. Flame, **161**(12), pp. 3063–3072.
[23] Hossain, M. M., Lu, G., and Yan, Y., 2011, "Three-Dimensional Reconstruction of Combustion Flames Through Optical Fiber Sensing and CCD Imaging," IEEE Instrumentation and Measurement Technology Conference (I2MTC), Binjiang, China, May 10–12.
[24] Dils, R., 1983, "High-Temperature Optical Fiber Thermometer," J. Appl. Phys., **54**(3), pp. 1198–1201.
[25] Bouguet, J.-Y., 2004, "Camera Calibration Toolbox for Matlab," http://www.vision.caltech.edu/bouguetj/calib_doc/
[26] Gruber, M., and Nejad, A., 1995, "New Supersonic Combustion Research Facility," J. Propul. Power, **11**(5), pp. 1080–1083.
[27] Kang, M., Li, X., and Ma, L., 2014, "Three-Dimensional Flame Measurements Using Fiber-Based Endoscopes," Proc. Combust. Inst., **35**(3), pp. 3821–3828.
[28] Kang, M., Wu, Y., and Ma, L., 2014, "Fiber-Based Endoscopes for 3D Combustion Measurements: View Registration and Spatial Resolution," Combust. Flame, **16**(12), pp. 3063–3072.
[29] Wickersham, A. J., Li, X., and Ma, L., 2014, "Advanced Methods for Extracting Flow and Combustion Physics From High Speed Laser Diagnostics," AIAA Paper No. 2014-1353.
[30] Berkooz, G., Holmes, P., and Lumley, J. L., 1993, "The Proper Orthogonal Decomposition in the Analysis of Turbulent Flows," Annu. Rev. Fluid Mech., **25**(1), pp. 539–575.
[31] Steinberg, A. M., Boxx, I., Stoehr, M., Carter, C. D., and Meier, W., 2010, "Flow-Flame Interactions Causing Acoustically Coupled Heat Release Fluctuations in a Thermo-Acoustically Unstable Gas Turbine Model Combustor," Combust. Flame, **157**(12), pp. 2250–2266.
[32] Stohr, M., Boxx, I., Carter, C. D., and Meier, W., 2012, "Experimental Study of Vortex-Flame Interaction in a Gas Turbine Model Combustor," Combust. Flame, **159**(8), pp. 2636–2649.
[33] Iudiciani, P., Duwig, C., Hosseini, S. M., Szasz, R., Fuchs, L., Gutmark, E., Lantz, A., Collin, R., and Aldén, M., 2010, "Proper Orthogonal Decomposition for Experimental Investigation of Swirling Flame Instabilities," AIAA Paper No. 2010-584.
[34] Caux-Brisebois, V., Steinberg, A. M., Arndt, C. M., and Meier, W., 2014, "Thermo-Acoustic Velocity Coupling in a Swirl-Stabilized Gas Turbine Model Combustor," Combust. Flame, **161**(12), pp. 3166–3180.
[35] Hilberg, D., Lazik, W., and Fiedler, H., 1993, "The Application of Classical Pod and Snapshot Pod in a Turbulent Shear Layer With Periodic Structures," *Eddy Structure Identification in Free Turbulent Shear Flows*, Springer, Dordrecht, pp. 251–259.
[36] Barber, T., Ahmed, H., and Shafi, N. A., 2005, "Pod Snapshot Data Reduction for Periodic Fluid Flows," AIAA Paper No. 2005-287.
[37] Feeny, B., and Kappagantu, R., 1998, "On the Physical Interpretation of Proper Orthogonal Modes in Vibrations," J. Sound Vib., **211**(4), pp. 607–616.
[38] Kostka, S., Lynch, A. C., Huelskamp, B. C., Kiel, B. V., Gord, J. R., and Roy, S., 2012, "Characterization of Flame-Shedding Behavior Behind a Bluff-Body Using Proper Orthogonal Decomposition," Combust. Flame, **159**(9), pp. 2872–2882.
[39] Wickersham, A. J., Li, X., and Ma, L., 2014, "Comparison of Fourier, Principal Component and Wavelet Analyses for High Speed Flame Measurements," Comput. Phys. Commun., **185**(4), pp. 1237–1245.
[40] Blanchard, R., Wickersham, A. J., Ma, L., Ng, W., and Vandsburger, U., 2014, "Simulating Bluff-Body Flameholders: On the Use of Proper Orthogonal Decomposition for Combustion Dynamics Validation," ASME J. Eng. Gas Turbines Power, **136**(12), p. 121504.
[41] Sundaram, S. S., and Babu, V., 2013, "Numerical Investigation of Combustion Instability in a V-Gutter Stabilized Combustor," ASME J. Eng. Gas Turbines Power, **135**(12), p. 121501.
[42] Sirovich, L., 1989, "Chaotic Dynamics of Coherent Structures," Phys. D, **37**(1), pp. 126–145.
[43] Cordier, L., and Tissot, G., 2014, "Model Reduction, POD and Data Assimilation," *Advanced Post-Processing of Experimental and Numerical Data*, von Karman Institute, Rhode-St-Genese, Belgium.
[44] Culick, F., 1987, "A Note on Rayleigh's Criterion," Combust. Sci. Technol., **56**(4–6), pp. 159–166.
[45] Lin, K.-C., Tam, C.-J., Boxx, I., Carter, C., Jackson, K., and Lindsey, M., 2007, "Flame Characteristics and Fuel Entrainment Inside a Cavity Flame Holder in a Scramjet Combustor," AIAA Paper No. 2007-5381.